Observing Conditions and Mid-IR Data Quality

Rachel Mason[a], Andre Wong[a, b], Tom Geballe[a], Kevin Volk[a], Tom Hayward[c], Matt Dillman[a], Scott Fisher[a], James Radomski[c].

[a]Gemini Observatory, Northern Operations Center, 670 N. A'ohoku Place, Hilo, HI, USA;
[b]Astronomy Department, P.O. Box 400325, University of Virginia, Charlottesville, VA, USA;
[c]Gemini Observatory, Southern Operations Center, c/o AURA, Casilla 603 La Serena, Chile

ABSTRACT

Ground-based mid-infrared (mid-IR) observations appear to be widely perceived as esoteric and demanding, and very sensitive to observing conditions. Although the principles of observing in the background-limited regime are well-known, it is difficult for the non-specialist to find specific information on exactly how mid-IR data can be affected by environmental conditions. Understanding these effects is important for the efficiency of mid-IR queue observing, the ability of classical observers to adapt their programs to the prevailing conditions, and the standard of data being delivered. Through operating mid-IR instruments in the queue at Gemini we have amassed a considerable database of standard star observations taken under a wide range of atmospheric conditions and in a variety of instrumental configurations. These data can be used to illustrate the effect of factors such as water vapour column, airmass, cloud cover, etc. on observed quantities like raw sky background, residual background, atmospheric transmission and image FWHM. Here we present some preliminary results from this study, which we hope to be of use to observatory users and staff as a guide to which environmental conditions are truly important to mid- IR imaging observations, and which can safely be neglected.

Keywords: infrared radiation, infrared instruments, atmospheric effects, observatory operations

1. INTRODUCTION

The mid-infrared spectral region covers a wide range of dust and molecular emission and absorption features, as well as many recombination and fine-structure lines, probing phenomena as diverse as star formation, stellar death (e.g. supernova remnants and planetary nebulae), and the dusty cores of active galactic nuclei. Although ground-based mid-IR instruments cannot match the exquisite sensitivity and wavelength coverage available to space-based satellites such as *Spitzer*, they can offer great advantages in spatial and spectral resolution, and often more complex observing modes (e.g. polarimetry and coronagraphy) than have been feasible for space-based instruments. Mid-infrared instruments currently or soon to be available on ground-based telescopes include Michelle[1] and T-ReCS[2] on the Gemini telescopes, VISIR[3] and MIDI[4] on ESO's Very Large Telescope, COMICS[5,6] on the Subaru telescope, MIRSI[7] at the IRTF, SpectroCam-10[8] at Palomar, visitor instruments TEXES[9] and MIRAC,[10] and CanariCam,[11] the mid-IR instrument about to be commissioned on the Gran Telescopio Canarias.

Making the most effective use of these instruments requires knowledge of how data quality is affected by environmental conditions. If, for example, sensitivity is seriously degraded by a high level of precipitable water vapour then it is wasteful to attempt observations on wet nights when optical instruments could be more profitably used instead. Equally, it makes little sense to schedule observations under the best conditions if similar quality data could be obtained with poorer seeing or cloudier skies. This kind of decision is particularly important in queue observing in which mid-IR instruments have to compete with other instruments for telescope time.

Some general information about the mid-IR sky is available in the literature,[12,13] as is some more specific work on sky noise and observing techniques.[14–17] However, we have been unable to find a basic and general treatment of how mid-IR sensitivity and image quality depend on environmental and other factors, especially

Further author information: (Send correspondence to R. E. M.)
R. E. M..: E-mail: rmason@gemini.edu@, Telephone: 1 808 974 2500

one based on an extensive set of real mid-IR data. We have therefore analysed a set of several hundred 10- and 20 μm imaging observations of standard stars to illustrate the effect of environmental conditions on mid-IR data quality. The conclusions presented here are drawn from data taken with Michelle on the Gemini North telescope on Mauna Kea, but they may be expected to apply broadly to similar instruments at other sites. Preliminary analysis of a similar data set from T-ReCS at Gemini South is consistent with the results in this paper.

2. MID-INFRARED OBSERVING FROM THE GROUND

Perhaps the defining characteristic of the ground-based mid-infrared is the huge level of thermal radiation from the sky, telescope and surroundings, which becomes the dominant source of background radiation beyond about 2.3 μm. According to Wien's displacement law, $\lambda T \sim 3000$ μm K, blackbody radiation from objects at $\sim$300 K reaches its maximum intensity in the 10 μm region. With a surface brightness of about -3 mag/sq arcsec around 11 μm, the sky itself is several orders of magnitude brighter than all but the brightest of astronomical sources.

Superimposed on the greybody curve of the continuum emission from the atmosphere and telescope is a forest of emission lines from telluric molecules, the dominant species being H_2O, O_3, CO_2, N_2O and CH_4.[13] These lines contribute emission and also represent regions of reduced atmospheric transparency (Fig. 1), so they both elevate the background in certain wavelength regions and increase the opacity of the atmosphere in those regions. The stronger H_2O lines can saturate in periods of high water vapour (and some are saturated even under "normal" conditions) while the weaker lines remain well fit by Gaussian or Voigt profiles. The effect on astronomical observations will depend on the filter or spectral range being used.

Because the mid-IR background is so large it must be subtracted before most astronomical objects can be detected, and the accuracy and uncertainty in the background subtraction is a limiting factor in the sensitivity of a mid-IR observation. The techniques generally used for background suppression, at least for imaging and low-resolution spectroscopic observations, are chopping and nodding. Chopping is tilting the telescope's secondary mirror by an amplitude corresponding to a few to a few tens of arcseconds on the sky, so that the first image contains the source + sky "A" and the second, source + sky "B" (with the source at a different location on the array, or only sky "B" if the chop amplitude exceeds the instrument's field of view). Subtraction of the "A" and "B" images leaves positive and negative images of the source, plus some level of residual background. If the chopping is working well then the residual background (the "radiative offset") results from the slightly different parts of the telescope seen by the detector at the two secondary mirror positions; imperfections on the primary mirror, for instance, will not subtract out perfectly through chopping alone. To cancel out this residual background the entire telescope is nodded periodically, typically every minute or so, often in the same direction and with the same amplitude as the chop. The nodding can also cancel out linear gradients in the sky background. Under many circumstances this scheme works remarkably well; compare for example the raw background levels in Fig. 2 and the final, subtracted background levels in Fig. 3. More details about chopping and nodding and a worked example can be found at www.gemini.edu/sciops/instruments/mid-ir-resources/mid-ir-observing; see also e.g. refs 16–18.

Power spectra of blank sky data obtained with very short integrations[16,17,19] have been used to investigate the timescales of the fluctuations of the sky background, with ref. 19 recommending chop frequencies of 0.5 Hz or above. The 1/f noise from the detector and temperature oscillations induced by the instrument's closed-cycle coolers must also be taken into account. For imaging observations chopping has traditionally taken place at a frequency of a few Hz, depending on the wavelength, observing site etc., This means that the secondary mirror is only stationary for $\sim$100 milliseconds between chops, and it is during this period that the detector is exposed and read out. Frame times (exposure times) for Michelle and T-ReCS are specified for normal observing conditions. In periods of particularly high background, which may be caused by clouds or a high water vapour column, the detectors may saturate; this tends to be how saturation occurs in the mid-IR, rather than on an astronomical source itself.

3. DATA AND REDUCTION

The data set presented here consists of Michelle observations of stars from the network of over 400 mid-IR standard stars established by M. Cohen and coworkers.[20] For any mid-IR imaging observation in the queue at

Table 1. Michelle imaging filters and standard star observations

Filter	Si-1	Si-2	Si-3	Si-4	Si-5	Si-6	N′	Qa
Central Wavelength (μm)	7.7	8.8	9.7	10.3	11.6	12.5	11.2	18.1
Number of Observations	40	70	50	32	130	80	212	245
Number of Observations in Clear Skies	29	58	38	24	104	65	165	202

Gemini, an observation of one of these standards is defined by the PI and obtained shortly before and/or after the science observation in the matching instrumental configuration. In-band flux densities for these standards were computed using the Cohen et al. stellar atmosphere models, integrated over the Michelle filter profiles*.

Michelle observations with an RA and Dec within .001 degrees of the coordinates of any of the standard stars were selected using an automatic routine from images available locally on hard disk and through the Gemini Science Archive. The images were reduced using the mireduce task in the Gemini IRAF package. The chop-nod observing scheme used for imaging observations results in files with as many extensions as nods (so a single ABBA nod sequence, for example, will have four extensions), with each extension containing three planes: one for the sum of the frames taken in chop beam A, one for chop beam B, and one for (chop A - chop B). Mireduce combines the data to yield a single "stacked" file containing a final background-subtracted image for the whole observation.

The IRAF package DAOPHOT was used to locate objects in the reduced images. For the standard star observations only a single object is expected in the 32 arcsec × 24 arcsec Michelle field of view, so any images yielding 2 or more objects were rejected, as were files with quality assessment header keywords marking them as bad for various reasons. Once an object in the image was identified, the analysis script would measure the full width at half maximum (FWHM), ellipticity, peak counts, and total flux of the object in an aperture of four times the measured FWHM. The Strehl ratio for each image was estimated by comparing the observed peak/total counts to theoretical maximum values for that ratio, calculated assuming an effective primary mirror diameter of 7.906 m, central obscuration of 0.129 m and pixel scale of 0.1005 arcsec/pixel. The instrumental responsivity in mJy/ADU was also derived, representing the amount of flux from an astronomical (or other) source required to produce 1 ADU at the detector. In addition to measurements made on the star itself, the mean value and standard deviation of the residual background in the sky annulus used by the photometry routine were also recorded. The raw sky background was taken as the mean of the raw background measured in each chop beam of each of the individual file extensions (nods).

Information about the weather conditions was extracted from several sources. The Gemini weather tower measures and writes information about ambient conditions (temperature, humidity, wind speed etc.) to the FITS header of each Michelle image. An assessment of the cloud cover, based on tools such as the counts measured by Gemini's guide probes and data supplied by the CFHT skyprobe†, is made by the nighttime summit observer and is also recorded in the headers. Atmospheric water vapour levels are recorded by the Caltech Submillimetre Observatory (CSO) in the form of the optical depth at 350 μm and 225 GHz and are available from the CSO website‡. In this paper we use: precipitable water vapour (mm) = $\tau_{225\mathrm{GHz}} \times 20.0$.

The final sample of standard star observations numbers approximately 860 spanning the time period between 2004 and 2007. Table 1 shows how the observations are distributed between the various imaging filters. The results in this paper are based on data taken in clear skies only.

4. EMISSION AND TRANSMISSION

Fig. 1 shows the atmospheric transmission[21] in the N and Q band windows at Mauna Kea and the profiles of some of the filters used by Michelle, T-ReCS and CanariCam. Some of the filters — particularly Qa and Si-1 —

*The flux densities and a tool for their calculation can be found at www.gemini.edu/sciops/instruments/mid-ir-resources

‡www.cfht.hawaii.edu/Instruments/Elixir/skyprobe/home.html

‡www.cso.caltech.edu/taumeter.txt

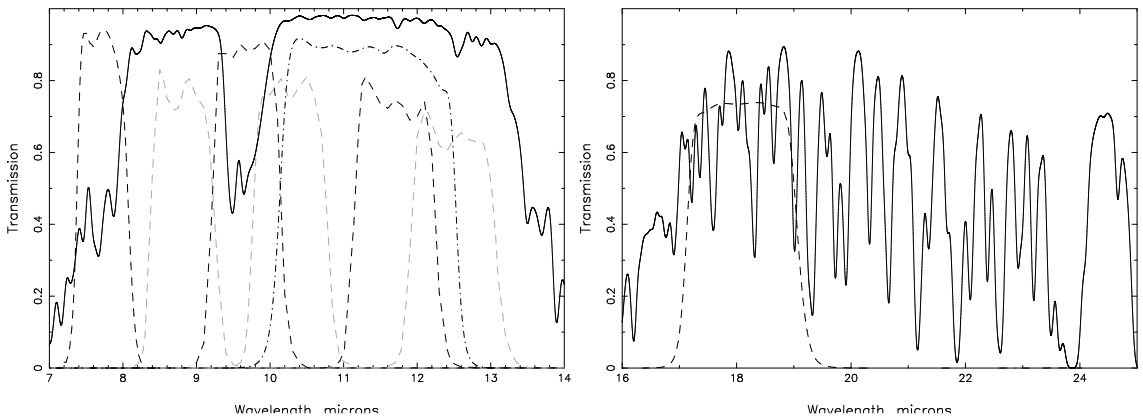

Figure 1. Left: N band atmospheric transmission (solid black line, calculated for 1.0 airmasses, 2.0 mm H_2O, 0.05 μm spectral resolution) and profiles of the Si-1 – Si-6 and N' filters used in Michelle and T-ReCS (see Table 1). Right: Q band atmospheric transmission (1.0 airmasses, 2.0 mm H_2O, 0.05 μm spectral resolution) and the Qa filter profile. The N band window is bounded by opaque H_2O and CO_2 lines and contains a strong telluric O_3 band around 9.6 μm, in the middle of the Si-3 filter. The transmission in the Q band "window" is generally poorer than in the N band because of the many strong and variable H_2O lines.

intersect regions of strong telluric H_2O lines, whereas others do not. This may be expected to cause differences in the background measured in each filter as a function of water vapour column (because line emission contributes to the background) and as differences in the amount and perhaps stability of the flux from a star as a function of water vapour column (because, for filters with water absorption bands within their bandpasses, more flux is transmitted when $\tau_{225\mathrm{GHz}}$ is low).

The raw background in the Michelle observations is shown in Fig. 2 as a function of 225 GHz optical depth. Not unexpectedly, linear least squares fits to the data show that the Qa filter is most sensitive to water vapour column, followed by Si-1, while there is least effect on the Si-2 data ($\sim$ 25% increase on going from $\tau_{225\mathrm{GHz}}$ = 0.05 to 0.15) . The Si-5 and Si-6 filters show a modest dependence on water vapour, with the background increasing by $\sim$30% with a threefold rise in $\tau_{225\mathrm{GHz}}$. The broader N$'$ filter, which encompasses the whole Si-5 and part of the Si-6 bandpasses, is similarly affected. The scatter in the Si-3 data seems reasonable, given that the peak of the filter transmission coincides with the strong and variable telluric O_3 feature. The similar scatter in the Si-4 filter may also be caused by the O_3 band, although that band only partially intersects the filter bandpass. Other factors that may be expected to affect the sky background to a greater or lesser degree include airmass, cloud cover (depending on the temperature of the clouds), ambient temperature, relative humidity and atmospheric dust and aerosols.[22] Additional causes of scatter in the relation between raw sky background and $\tau_{225\mathrm{GHz}}$ may include emission from species other than H_2O and $\tau_{225\mathrm{GHz}}$ not being a good indicator of the water vapour column along the particular line of sight of the observations.

Saturation in Michelle imaging data occurs at $\sim$55,000 ADU. Fig. 2 shows that with the current exposure times saturation due to high water vapour levels is unlikely in the Si-2, Si-4, Si-5 and Si-6 filters on most nights on Mauna Kea, but with these particular exposure times it would be unwise to attempt observations in the Si-1, Si-3, N' and Qa filters when the PWV is much above 3 mm (note that a bias level of about 5000 ADU has been subtracted off the raw counts). Cloudy conditions can also cause saturation of the images.

Apart from the risk of saturation, a reason to be concerned about the background level is its effect on the sensitivity of the observations and the ability to detect faint objects. Assuming that the dominant source of noise is the random fluctuations in the photons from the sky and telescope themselves (the background limited case), the pixel-to-pixel variations in the residual background (after chop and nod subtraction) will be proportional to the square root of the counts in the raw background. Fig. 3 shows that the mean residual background is low for all measured values of the precipitable water vapour in all filters. Evidently the chopping and nodding can reduce the overall background level by a factor of $>10^4$ in the sky-subtracted frames even for relatively high water

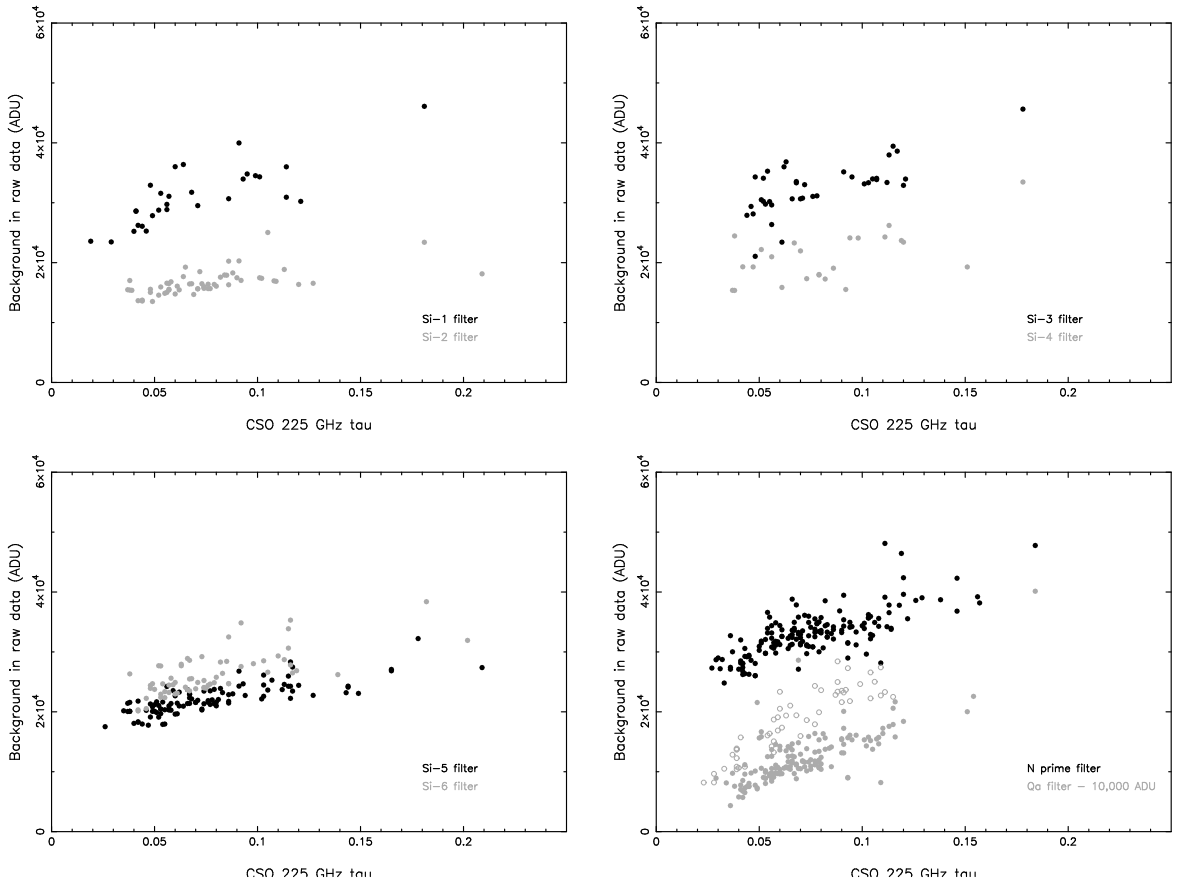

Figure 2. Bias-subtracted raw background vs 225 GHz optical depth for various filters. The solid and open symbols for the Qa data represent frame times of 20 and 30 ms, used before and after March 2007 respectively.

vapour columns where the background might be expected to be more variable. Fits to the standard deviation of the mean residual background, however, do reveal some dependence on $\tau_{225\mathrm{GHz}}$ (Fig. 4). The scatter in the data and the limited range of $\tau_{225\mathrm{GHz}}$ covered by the observations make it difficult to draw firm quantitative conclusions, but in the N′ filter, for instance, a factor of 1.33 increase in the raw background counts corresponds to a rise of roughly a factor of 1.13 in the standard deviation of the residual background counts.

A few files with standard deviations >1.1 were removed from Fig. 4. These files were visually inspected and found to contain strong artefacts as a result of the very bright standard stars used in these observing programs. Such artefacts are well known in arrays of this type (see ref. 23 for a description and some examples). Weaker artefacts from fainter stars may account for some of the scatter in the remaining data, as may low-level electronic noise (not removed from the data for this analysis), and the variations in the effectiveness of the nod at removing the radiative offset and gradients in the sky background.

So far we have been dealing with the effects of increased background *emission*, but periods of high precipitable water vapour will also be periods of increased atmospheric *opacity*, at least in spectral regions with strong and/or numerous water lines. One gauge of the atmospheric opacity, all else being equal, is the flux density of a source required to cause a detector response of 1 ADU, shown in Fig. 5 as a function of $\tau_{225\mathrm{GHz}}$, and in Fig. 6 as a function of airmass. For the Si-2, Si-5, Si-6 and N' filters the responsivity is fairly flat with little scatter in both plots. For the Si-1, Si-3, Si-4 and Qa filters, however, there is much more scatter and — in the case of Qa and (probably) Si-1— a trend with τ_{225GHz}. The behaviour of the former set of filters is in line with what would be expected based on Fig. 1, given that all of these filters are comparatively free of strong water lines. Qualitatively, the dependence of the Qa and Si-1 responsivity on the atmospheric water vapour is also unsurprising. As with

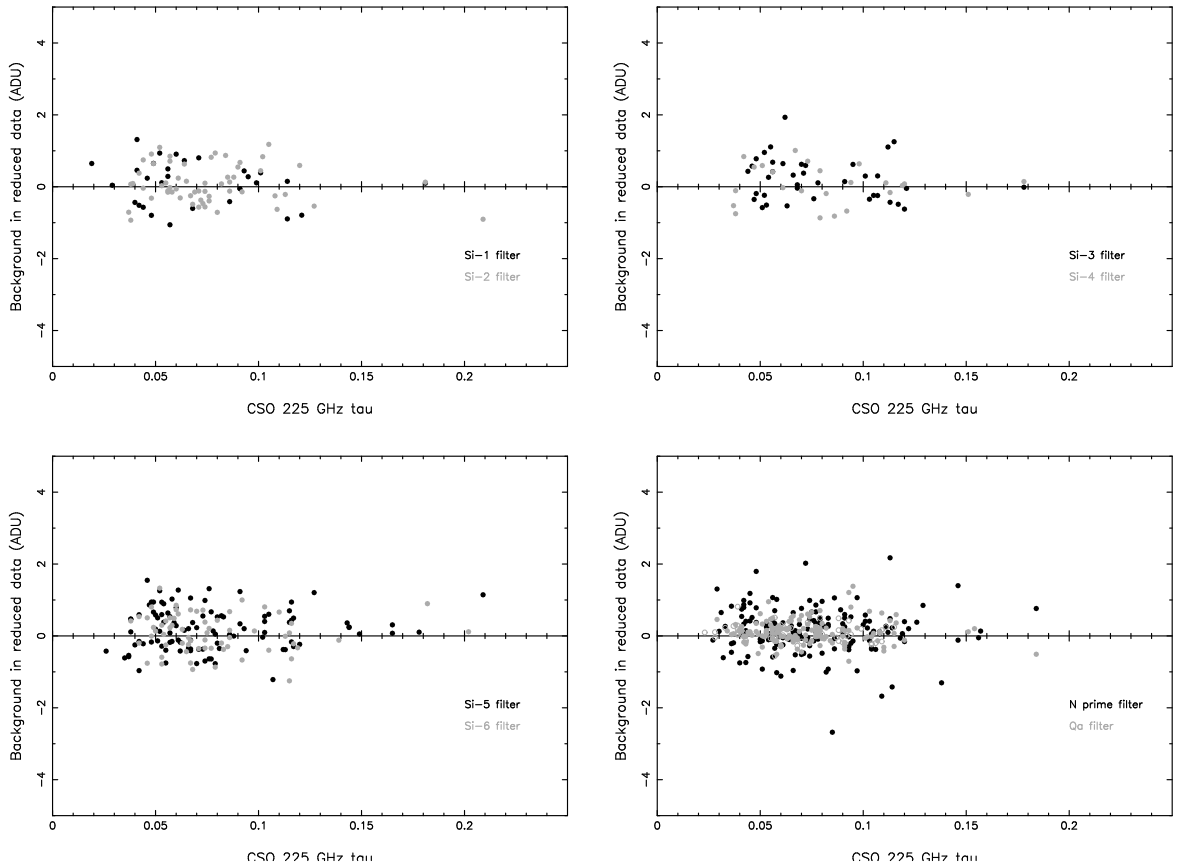

Figure 3. Mean residual background in an annulus around the star, measured on the final "reduced" image (§3).

the raw background, the scatter in the responsivity data for Si-3 and Si-4 probably results from the telluric O_3 band.

Fig. 6 reveals almost no dependence of responsivity on airmass for the Si-2, Si-5, Si-6 and N′ filters, while there may be a weak effect in Si-1, Si-3 and Qa. Again, this is qualitatively what would be expected from Fig. 1. Quantitatively, the airmass dependence will be related to the number of lines present and their profiles; if a few strongly saturated lines are present the extinction is predicted to vary as the square-root of the airmass, rather than being exponential with airmass – a linear extinction law in magnitudes – as is the case for only unsaturated lines. There are enough data points in the Qa filter to attempt to separate the effects of airmass and water vapour on the responsivity. The Qa points in Fig. 6 include only data taken at $\tau_{225\mathrm{GHz}}$ <0.07 but the scatter is still large. Some of this may be due to the fact that the responsivity changes measurably over even this limited range of $\tau_{225\mathrm{GHz}}$, but it is also likely that the Qa filter is also sensitive to other variables such as temperature and humidity, and to variations in the water vapour column for different lines of sight.

Although it is difficult to disentangle the effects of airmass and water vapour in the data, especially for the filters with fewer data points, we can make a crude estimate of the effect of those quantities on the transmission and signal-to-noise ratio (S/N) using atmospheric models[21] and the relation

$$S/N \propto \frac{T}{((1-T)+0.04)^{0.5}}$$

where T is the atmospheric transmission integrated over the filter bandpass (and therefore $1-T$ the emissivity of the atmosphere), and 0.04 is a 4% assumed telescope and instrument emissivity. The results of these calculations are shown in Table 2.

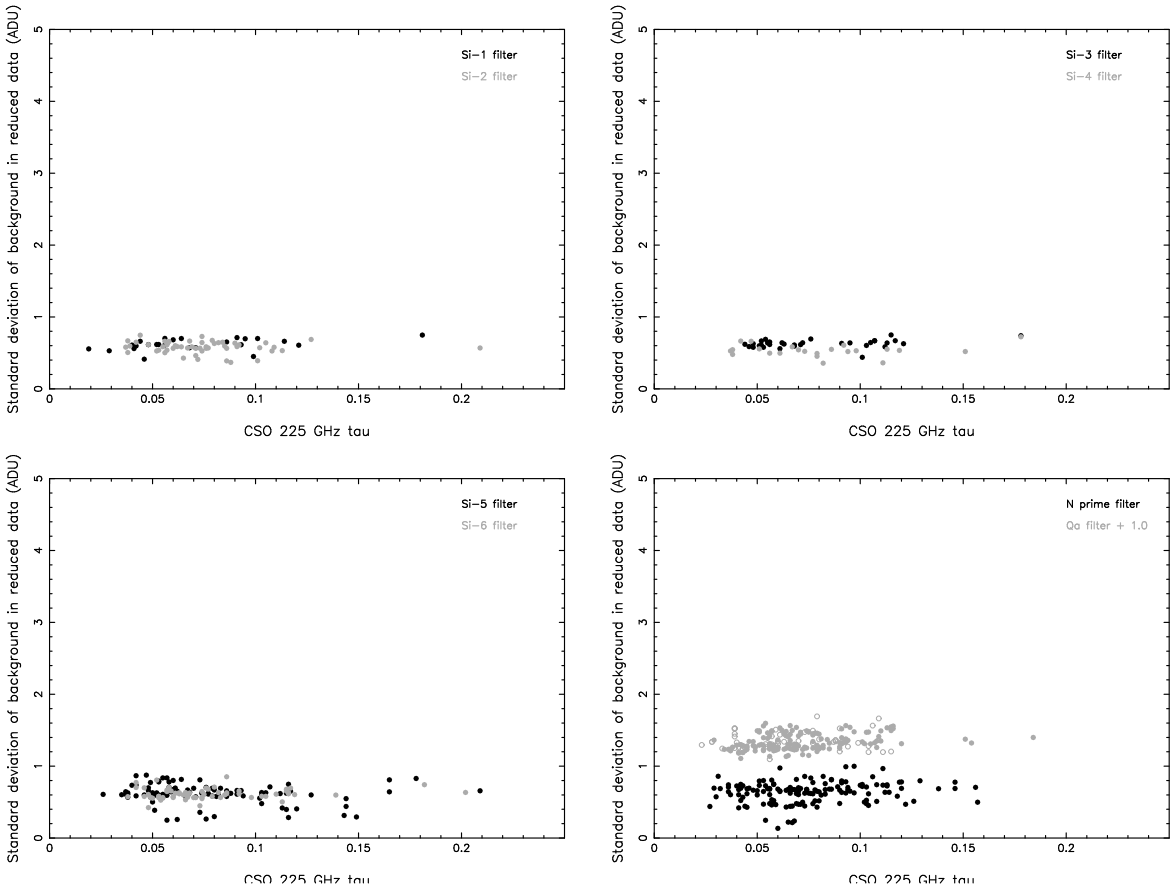

Figure 4. Standard deviation of the residual background in an annulus around the star. As in Fig. 2, the solid and open grey symbols represent Qa data taken with different frame times.

The implications of these data depend on the kind of observations being attempted. The PI of a program mapping the morphology of a bright HII region at high spatial resolution in the Si-5 filter may find the slight decrease in sensitivity at high water vapour columns acceptable, given that 1mm of precipitable water vapour occurs only $\sim 20\%$ of the time even at a dry site like Mauna Kea. For a program aiming to detect a faint AGN, on the other hand, the increased sky background and lower transmission will be more important, especially in the Q band. It is for programs like these that systematic effects such as the stability of the nod subtraction (particularly close to zenith where the telescope pupil is rotating at is fastest rate) and electronic noise will also become important in determining the limiting sensitivity reached for a given observation.

4.1 IMAGE QUALITY

A great benefit of observing in the mid-IR from the ground is that the effect of seeing is minimal at these wavelengths (particularly in the Q band), and near-diffraction limited images are routinely obtained. For an 8 m telescope this implies FWHM$\sim$0.3 arcsec, depending on the observing wavelength.

Fig. 7 shows the FWHM and Strehl ratio in the various Michelle filters as function of airmass. Compared with optical wavelengths, where an airmass$^{0.6}$ dependence is expected, the FWHM of the Michelle images shows only a weak dependence on the airmass. Subjectively this agrees with our experience of long integrations on certain science targets, but examples of a small change in mid-IR FWHM with airmass are known.[24]

The FWHM measured in the Qa filter are strongly concentrated towards the diffraction limit in Fig. 7, but those measured in the shortest wavelength filters show more scatter. This may reflect atmospheric effects starting to become important at the shorter wavelengths. As there is no generally-available DIMM on Mauna

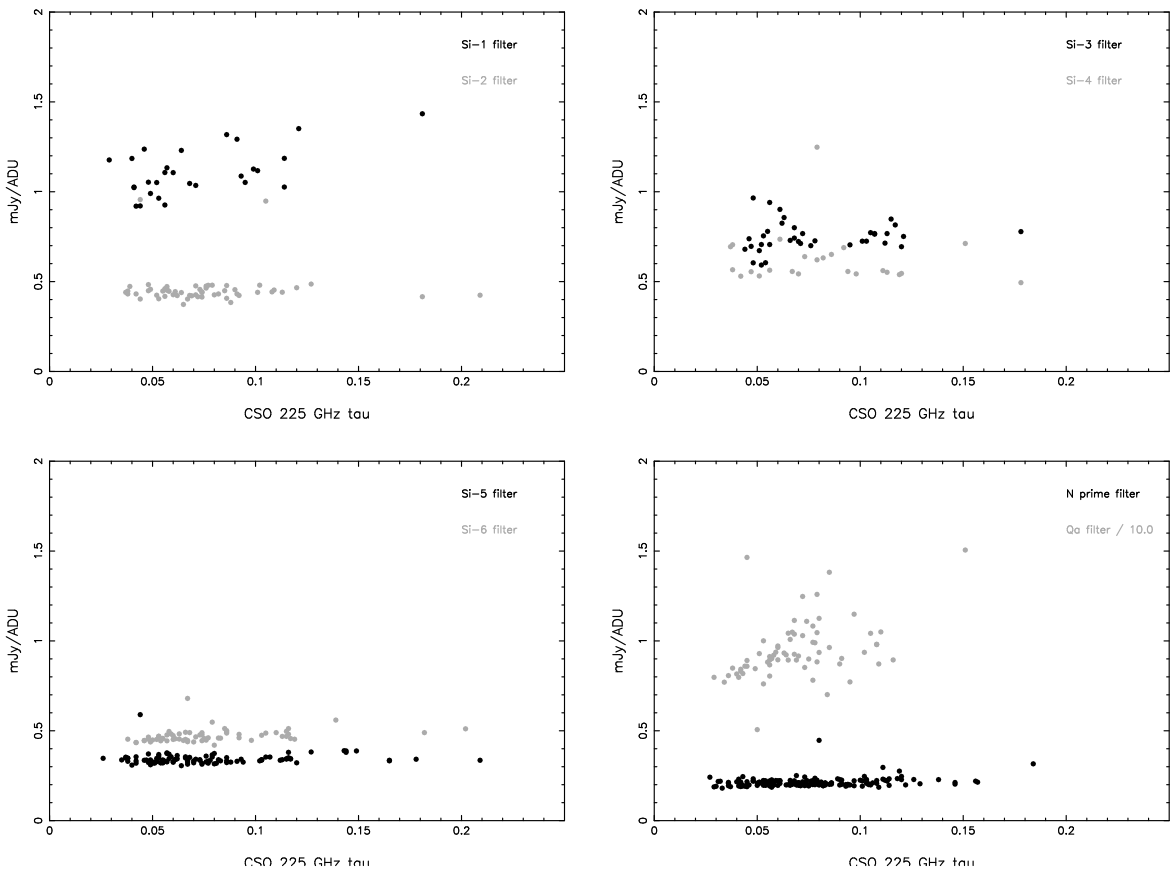

Figure 5. Responsivity for various filters as a function of precipitable water vapour. To separate the effects of water vapour and airmass the Qa plot shows only data taken at 1.0 - 1.2 airmasses. For clarity only the 30 ms frame time is shown.

Kea, we do not have measurements of the optical seeing at the time of the Michelle observations to investigate the relation between the optical seeing and the mid-IR FWHM. However, analysis of T-ReCS data shows little or no dependence of the FWHM in the Si-2, Si-5 and Qa filters on optical seeing, except in the poorest conditions. The VISIR User Manual[§]also shows plots of FWHM at N and Q against the optical seeing, again showing only a weak dependence.

High Strehl ratios are certainly possible, especially in the Qa filter where Strehl ratios of 80% are not uncommon, but are generally lower in the shorter wavelength filters. There may be a trend of lower Strehl ratios at higher airmasses but the present data do not allow unambiguous conclusions to be drawn. Although the FWHM are fairly constant, a wide range of Strehl ratios is observed. The variation in Strehl ratios probably reflects errors in measuring the peak and total counts in the star and the performance of the telescope and its subsystems under the stress of chopping, rather than being directly related to the conditions at the time of the observations.

5. SUMMARY

Perceiving a lack of easily-accessible information about observing conditions and mid-IR data, we have compiled a set of Michelle imaging observations which we use to illustrate some of these effects. As expected, the raw background is sensitive to the atmospheric water vapour column. Although chopping and nodding leave only a

[§]http://www.eso.org/sci/facilities/paranal/instruments/visir/

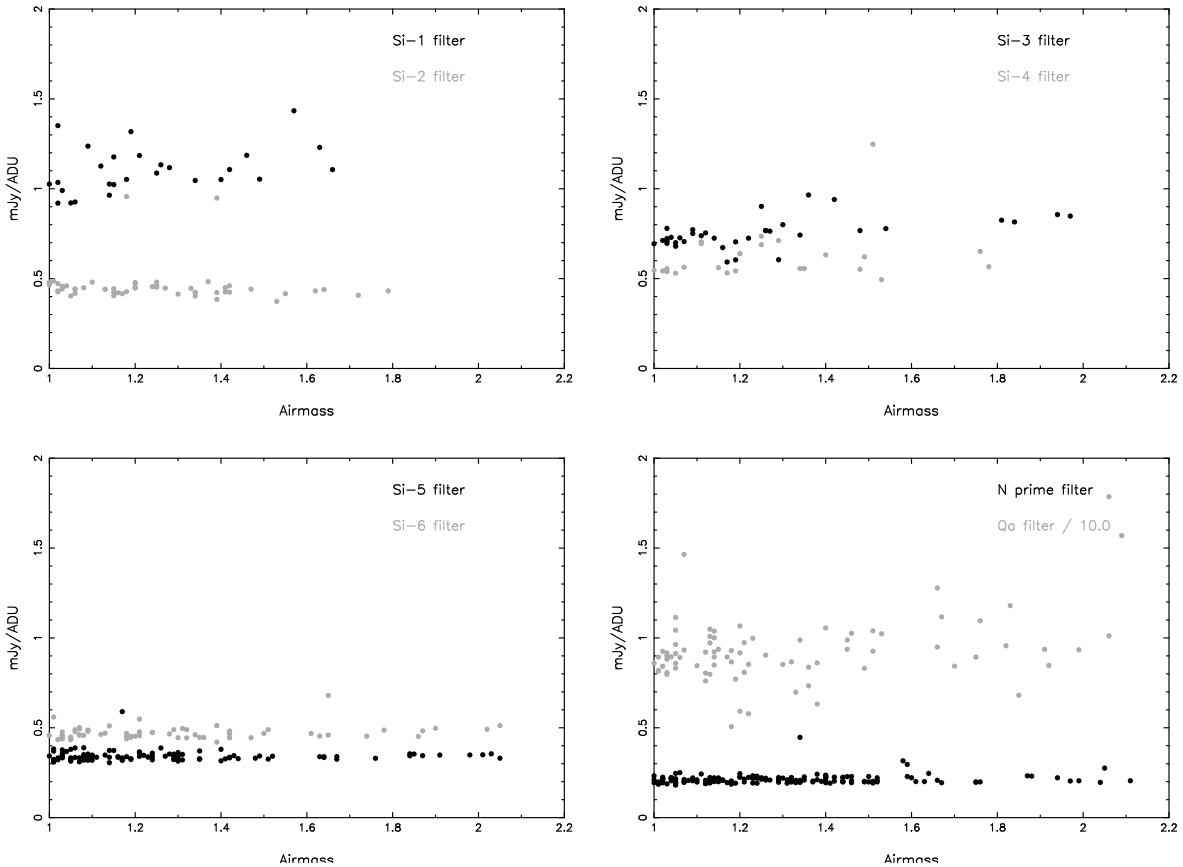

Figure 6. Responsivity for various filters as a function of airmass. To separate the effects of water vapour and airmass the Qa plot shows only data with $\tau_{225\mathrm{GHz}}$ <0.07. For clarity only the 30 ms frame time is shown.

small level of residual background under all conditions studied, the noise in that residual background does have some dependence on the raw background level, albeit with considerable scatter. The magnitude of these effects varies considerably from filter to filter, with those intersecting strong telluric lines being more affected than those in "clean" regions of the atmosphere. In the longer wavelength filters the image FWHM is usually close to the diffraction limit. The larger scatter at shorter wavelengths may be due to the greater importance of seeing in that region. Unlike in the optical, we see little dependence of FWHM on airmass.

We hope that this serves as a useful basic aid to understanding how environmental conditions affect ground-based mid-IR imaging observations. At Gemini, this information will be used to evaluate and improve observing and quality assessment procedures for mid-IR data. In the future we plan to expand the analysis to cover more aspects of imaging data, as well as spectroscopic and polarimetric data sets.

ACKNOWLEDGMENTS

We would like to thank Ruisheng Peng at CSO and Glenn Morrison at CFHT for helpful information about those observatories' environmental monitoring equipment. The Gemini Observatory is operated by the Association of Universities for Research in Astronomy, Inc., under a cooperative agreement with the NSF on behalf of the Gemini partnership: the National Science Foundation (United States), the Science and Technology Facilities Council (United Kingdom), the National Research Council (Canada), CONICYT (Chile), the Australian Research Council (Australia), Ministério da Ciência e Tecnologia (Brazil), and SECYT (Argentina)

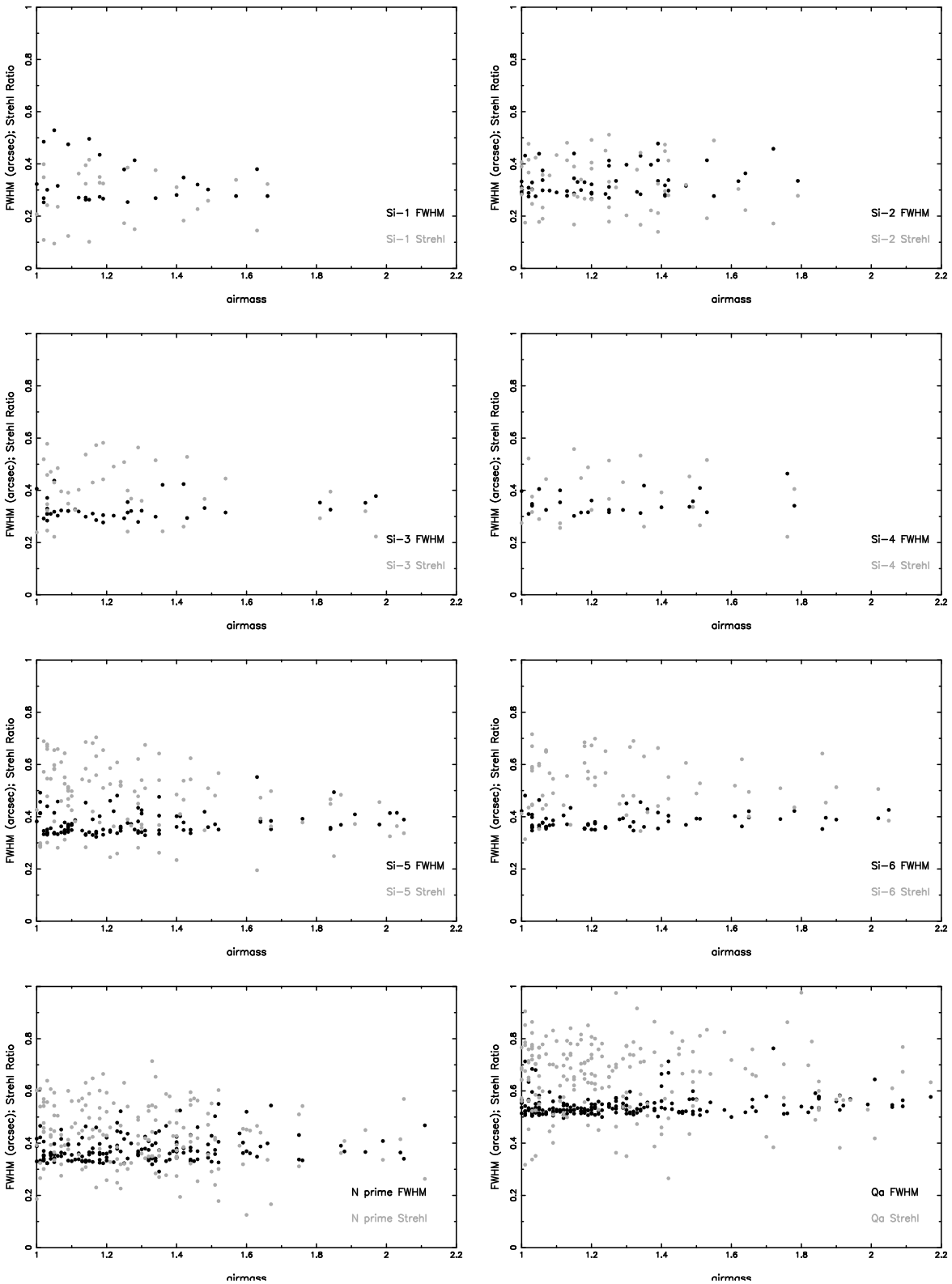

Figure 7. FWHM and Strehl ratio for various filters as a function of airmass.

Table 2. Transmission and S/N for various airmasses and water vapour columns (see text for details of the calculations)

Airmass	Transmission					S/N (normalised to secz=1.0, 1.0 mm H_2O)			
	1.0 mm	1.6 mm	3.0 mm	5.0 mm		1.0 mm	1.6 mm	3.0 mm	5.0 mm
					Si-1				
1.0	0.64	0.61	0.55	0.51		1.00	0.92	0.78	0.69
1.5	0.57	0.54	0.48	0.43		0.82	0.75	0.63	0.54
2.0	0.52	0.48	0.43	0.38		0.71	0.63	0.54	0.46
					Si-2				
1.0	0.95	0.95	0.93	0.92		1.00	0.95	0.87	0.81
1.5	0.94	0.93	0.91	0.89		0.89	0.84	0.76	0.70
2.0	0.92	0.91	0.88	0.86		0.81	0.76	0.69	0.63
					Si-3				
1.0	0.73	0.73	0.72	0.72		1.00	0.99	0.98	0.97
1.5	0.67	0.67	0.66	0.66		0.85	0.84	0.83	0.81
2.0	0.63	0.62	0.62	0.61		0.75	0.74	0.73	0.71
					Si-4				
1.0	0.93	0.93	0.92	0.92		1.00	0.99	0.96	0.93
1.5	0.91	0.90	0.90	0.89		0.89	0.88	0.85	0.82
2.0	0.89	0.88	0.87	0.86		0.82	0.81	0.78	0.74
					Si-5				
1.0	0.98	0.98	0.97	0.96		1.00	0.96	0.89	0.83
1.5	0.98	0.97	0.96	0.95		0.92	0.88	0.80	0.74
2.0	0.97	0.96	0.95	0.93		0.86	0.82	0.74	0.67
					Si-6				
1.0	0.95	0.94	0.93	0.91		1.00	0.95	0.87	0.81
1.5	0.93	0.92	0.90	0.88		0.87	0.83	0.75	0.70
2.0	0.91	0.90	0.88	0.85		0.79	0.74	0.67	0.62
					N′				
1.0	0.98	0.98	0.97	0.96		1.00	0.97	0.91	0.84
1.5	0.97	0.97	0.96	0.95		0.93	0.88	0.81	0.75
2.0	0.97	0.96	0.94	0.93		0.86	0.82	0.75	0.69
					Qa				
1.0	0.78	0.73	0.64	0.56		1.00	0.86	0.66	0.53
1.5	0.72	0.66	0.56	0.48		0.83	0.70	0.53	0.42
2.0	0.68	0.61	0.49	0.41		0.74	0.61	0.43	0.34

REFERENCES

[1] A. C. Glasse, E. I. Atad-Ettedgui, and J. W. Harris. "Michelle Midinfrared Spectrometer and Imager". In *Proc. SPIE Vol. 2871, p. 1197-1203 (1997).*

[2] C. M. Telesco, R. K. Pina, K. T. Hanna, J. A. Julian, D. B. Hon, and T. M. Kisko. "GatirCam: Gemini mid-infrared imager". In *Proc. SPIE Vol. 3354, p. 534-544 (1998).*

[3] P.-O. Lagage, G. A. Durand, C. Lyraud, Y. Rio, J.-W. Pel, and J. C. de Haas. "Final design of VISIR: the mid-infrared imager and spectrometer for the VLT". In *Proc. SPIE Vol. 4008, p. 1120-1131 (2000).*

[4] C. Leinert, U. Graser, F. Przygodda, L. B. F. M. Waters, G. Perrin, W. Jaffe, B. Lopez, E. J. Bakker et al. "MIDI - the 10 μm instrument on the VLTI". *Ap&SS*, 286:73–83, 2003.

[5] H. Kataza, Y. Okamoto, S. Takubo, T. Onaka, S. Sako, K. Nakamura, T. Miyata, and T. Yamashita. "COMICS: the cooled mid-infrared camera and spectrometer for the Subaru telescope". In *Proc. SPIE Vol. 4008, p. 1144-1152 (2000).*

[6] Y. K. Okamoto, H. Kataza, T. Yamashita, T. Miyata, S. Sako, S. Takubo, M. Honda, and T. Onaka. "Improved performances and capabilities of the Cooled Mid-Infrared Camera and Spectrometer (COMICS) for the Subaru Telescope". In *Proc. SPIE, Volume 4841, pp. 169-180 (2003).*

[7] L. K. Deutsch, J. L. Hora, J. D. Adams, and M. Kassis. "MIRSI: a Mid-InfraRed Spectrometer and Imager". In *Proc. SPIE, Volume 4841, pp. 106-116 (2003).*

[8] T. L. Hayward, J. E. Miles, J. R. Houck, G. E. Gull, and J. Schoenwald. "SpectroCam-10: a 10-um spectrograph/camera for the Hale Telescope". In *Proc. SPIE Vol. 1946, p. 334-340 (1993).*

[9] J. H. Lacy, M. J. Richter, T. K. Greathouse, D. T. Jaffe, Q. Zhu, and C. Knez. "TEXES: sensitive and versatile spectrograph for mid-infrared astronomy". In *Proc. SPIE, Volume 4841, pp. 1572-1580 (2003).*

[10] W. F. Hoffmann, G. G. Fazio, K. Shivanandan, J. L. Hora, and L. K. Deutsch. "MIRAC: a mid-infrared array camera for astronomy". In *Proc. SPIE Vol. 1946, p. 449-460 (1993).*

[11] C. M. Telesco, D. Ciardi, J. French, C. Ftaclas, K. T. Hanna, D. B. Hon, J. H. Hough, J. Julian, et al. "CanariCam: a multimode mid-infrared camera for the Gran Telescopio CANARIAS". In *Proc. SPIE, Volume 4841, pp. 913-922 (2003).*

[12] I. S. Glass. *Handbook of Infrared Astronomy.* Highlights of Astronomy, 1999.

[13] A. Tokunaga. *Allen's Astrophysical Quantities.* Springer, 1999.

[14] F. J. Low and G. H. Rieke. "The instrumentation and techniques of infrared photometry.". In *Astrophysics. Part A: Optical and Infrared*, pages 415–462, 1974.

[15] S. Bensammar. "Statistical properties of atmospheric emission in the infrared. II - Atmospheric noise correlation". *A&A*, 65:199–205, 1978.

[16] R. Papoular. "The processing of infrared sky noise by chopping, nodding and filtering". *A&A*, 117:46–52, 1983.

[17] H. U. Kaeufl, P. Bouchet, A. van Dijsseldonk, and U. Weilenmann. "A sky-noise measurement and its implication for ground-based infrared astronomy in the 10-micron atmospheric window". *Experimental Astronomy*, 2:115–122, 1991.

[18] M. Bertero, P. Boccacci, and M. Robberto. "Wide-Field Imaging at Mid-Infrared Wavelengths: Reconstruction of Chopped and Nodded Data". *PASP*, 112:1121–1137, 2000.

[19] T. Miyata, H. Kataza, Y. Okamoto, T. Tanabé, T. Onaka, T. Yamashita, K. Nakamura, and H. Shibai. "MICS: A New Mid-Infrared Camera and Spectrometer for Ground-based Astronomy". *PASP*, 111:750–764, 1999.

[20] M. Cohen, R. G. Walker, B. Carter, P. Hammersley, M. Kidger, and K. Noguchi. "Spectral Irradiance Calibration in the Infrared. X. A Self-Consistent Radiometric All-Sky Network of Absolutely Calibrated Stellar Spectra". *AJ*, 117:1864–1889, 1999.

[21] S. D. Lord. Nasa technical memorandum 103957, 1992.

[22] C. H. Smith and D. A. Harper. "Mid-Infrared Sky Brightness Site Testing at the South Pole". *PASP*, 110:747–753, 1998.

[23] S. Sako, Y. K. Okamoto, H. Kataza, T. Miyata, S. Takubo, M. Honda, T. Fujiyoshi, T. Onaka, and T. Yamashita. "Improvements in Operating the Raytheon 320 × 240 Pixel Si:As Impurity Band Conduction Mid-Infrared Array". *PASP*, 115:1407–1418, 2003.

[24] J. T. Radomski, C. Packham, N. A. Levenson, E. Perlman, L. L. Leeuw, H. Matthews, R. Mason, J. M. De Buizer, C. M. Telesco, and M. Orduna. Gemini Imaging of Mid-IR Emission from the Nuclear Region of Centaurus A. *ArXiv 0802.4119*, 2008.